

Article

Numerical Simulation of Flow and Argon Bubble Distribution in a Continuous Casting Slab Mold under Different Argon Injection Modes

Zexian He ¹, Qiao Cheng ¹, Haibiao Lu ¹, Yunbo Zhong ¹, Changgui Cheng ^{2,3}, Jingxin Song ^{4,*} and Zuosheng Lei ^{1,*}

- ¹ State Key Laboratory of Advanced Special Steel & Shanghai Key Laboratory of Advanced Ferrometallurgy, Shanghai University, Shanghai 200444, China; hezexian0108@shu.edu.cn (Z.H.); chengnine@shu.edu.cn (Q.C.); luhaibiao@shu.edu.cn (H.L.); yunboz@staff.shu.edu.cn (Y.Z.)
- ² The State Key Laboratory of Refractories and Metallurgy, Wuhan University of Science and Technology, Wuhan 430081, China; ccghlx@wust.edu.cn
- ³ Hubei Provincial Key Laboratory for New Processes of Ironmaking and Steelmaking, Wuhan University of Science and Technology, Wuhan 430081, China
- ⁴ Baosteel Central Research Institute Meishan R&D Center, Nanjing 210039, China
- * Correspondence: songjingxin@baosteel.com (J.S.); lei_zsh@staff.shu.edu.cn (Z.L.)

Abstract: A three-dimensional model is established to investigate the effect of argon injection mode, argon flow rate and casting speed on the gas–liquid two-phase flow behavior inside a slab continuous casting mold. The Eulerian–Eulerian model is employed to simulate the gas–liquid flow, and the population balance model is applied to describe the bubble breakage and coalescence process in the mold. The numerical simulation results of the bubble size distribution are verified using the water model experiment. The results show that the flow field and bubble distribution are similar between the argon injection at the upper submerged entry nozzle (SEN) and tundish upper nozzle (TUN), while the number density is larger for the argon injection of TUN. The coalescence rate of bubbles and the bubble size inside the mold increase with increasing argon flow rate. When the argon flow rate exceeds 4 L/min, the flow pattern of liquid steel changes from double-roll flow to complex flow, with aggravation of the level fluctuation of the top surface near the SEN. When the casting speed increases, the bubble breakup rate increases and results in a decrease in the size of bubbles inside the mold. At a high casting speed, the flow pattern tends to form double-roll flow, and the liquid level at the narrow face of the top surface increases.

Keywords: continuous casting; argon injection mode; numerical simulation; bubble size distribution; population balance model



Citation: He, Z.; Cheng, Q.; Lu, H.; Zhong, Y.; Cheng, C.; Song, J.; Lei, Z. Numerical Simulation of Flow and Argon Bubble Distribution in a Continuous Casting Slab Mold under Different Argon Injection Modes. *Metals* **2023**, *13*, 2010. <https://doi.org/10.3390/met13122010>

Academic Editors: Paolo Ferro and Alessandro Morri

Received: 27 November 2023
Revised: 10 December 2023
Accepted: 12 December 2023
Published: 14 December 2023



Copyright: © 2023 by the authors. Licensee MDPI, Basel, Switzerland. This article is an open access article distributed under the terms and conditions of the Creative Commons Attribution (CC BY) license (<https://creativecommons.org/licenses/by/4.0/>).

1. Introduction

During the slab continuous casting process, argon gas is usually injected into the nozzle to prevent the nozzle clogging. Generally, there exist three types of argon injection modes, including injection from the stopper rod, tundish upper nozzle (TUN) and submerged entry nozzle (SEN) [1–3]. After entering the slab mold, the argon gas plays a significant role in removing nonmetallic inclusions, making the liquid steel composition and temperature uniform, controlling the flow and multiphase reaction, etc. [4–6]. Meanwhile, the argon bubbles break and collapse into different sizes, and the size directly influences the final slab quality. Large bubbles will aggravate liquid-level fluctuation and increase the risk of slag entrainment, while small bubbles are likely to move together with the liquid steel flow, and finally become captured by the solidified shell to form surface defects, such as slivers and pinholes. Therefore, it is of great significance to study the bubble size distribution and bubble transport in the slab mold for control of the liquid steel fluid and to improve slab quality.

In recent decades, extensive works have been conducted to investigate the transport behavior of bubbles and distribution of bubble size within a mold through the water model. Bai et al. [7] studied the bubble formation during argon blowing at the tundish upper nozzle, and the results show that bubble size increases with increasing gas flow rate and decreasing liquid flow rate. Wu et al. [8] used a high-speed camera and laser to study bubble trajectory, velocity and size distribution in a slab mold. They found that the influence of gas flow rate on the number of bubbles is much more significant than that of the water flow rate. Thomas et al. [9] investigated bubble formation, breakage, coalescence and accumulation by using argon injection at a stopper rod with multiple side-channels. However, only limited information about the bubble breakage and coalescence process in the slab mold can be obtained through the water model experiment.

With the development of computer technology, numerical simulation has become an effective method to investigate the multiphase flow in slab continuous casting molds [10,11]. For the gas–liquid two-phase flow, the Eulerian–Eulerian approach and Eulerian–Lagrange approach are the most widely used numerical methods [12]. In the first method, the argon bubbles are treated as a continuous phase, while in the second one, the argon bubbles are set as a discrete phase [13,14]. Liu et al. [15] used the Eulerian–Lagrange approach to simulate the liquid steel flow in a continuous casting mold, and the distribution of bubble size obtained from the water model. The results show that larger bubbles easily float near the SEN, and cause the lifting flow in this region, while small bubbles can move to the mold's narrow face along with the jet flow. Chen et al. [16] also used the same approach to study the effect of argon flow rate on the liquid steel flow pattern and bubble distribution. They successfully predicted the transformation of the flow pattern from the double-roll to complex flow and single-roll with increasing argon flow rate, and found that most argon bubbles float near the SEN and lead to excessive level fluctuation. However, both of the aforementioned models do not consider the bubble breakage and coalescence process. In recent years, Liu and his co-workers [17–20] employed the population balance model (PBM) based on the Eulerian–Eulerian method to investigate the poly-dispersed bubble flow in the slab mold, and successfully predicted the bubble breakage and coalescence process in the mold. The results indicated that the proportion of large bubbles and average bubble diameter in the upper recirculation zone decreased with the increment of water flow rate and increased with the increment of gas flow rate. Meanwhile, similar conclusions were also reached by Zhang [21]: it was confirmed that increasing argon gas flow rate promotes bubble breakage, and increasing casting speed promotes bubble coalescence. The aforementioned study has great significance in understanding the flow pattern and bubble distribution within a mold under argon injection; however, most of these works injected the argon through the top of the SEN inlet. As a matter of fact, argon bubbles are commonly injected into slab molds from the stopper rod, the tundish upper nozzle or the submerged entry nozzle. The argon injection modes affect the bubble size distribution, bubble breakage and coalescence process in the mold. However, the numerical investigations of the influence of argon injection modes on the bubble breakage and coalescence process in the slab continuous casting mold have not been reported.

The aim of this study is to elucidate the effect of the argon injection modes on the argon bubble distribution and to choose the optimal argon injection mode to investigate the flow and argon bubble distribution under different process parameters. A three-dimensional slab model is established to investigate the flow and the characteristics of bubble distribution in the slab mold. The Eulerian–Eulerian model is employed to simulate the gas–liquid flow, and the PBM is applied to describe the bubble breakage and coalescence process in the mold. By comparing the water model experimental results, the accuracy of our calculation model is determined. The effects of argon injection mode, argon flow rate and casting speed on the flow field, as well as the bubble size and number density are analyzed and discussed.

2. Mathematical Modeling

In the current model, the Euler–Euler method is used to investigate the gas–liquid two-phase flow within the mold; the liquid steel and argon gas are treated as a continuous phase. The breakage and coalescence of argon bubbles are considered by using the PBM. The detailed descriptions are listed as follows.

2.1. Assumptions

In order to simplify the complex gas–liquid flow in the mold, the following assumptions are made:

- (1) The liquid steel and argon gas are treated as incompressible Newtonian fluids, each phase occupying a common space area and having its own velocity field.
- (2) The influence of liquid slag on the liquid steel flow is ignored.
- (3) Solidification and heat transfer are not considered.
- (4) The influence of mold taper and oscillation are neglected.

2.2. Governing Equations

2.2.1. Continuity and Momentum Equations

The continuity equation and momentum equation are as follows:

$$\frac{\partial}{\partial t}(\alpha_h \rho_h) + \nabla \cdot (\alpha_h \rho_h \vec{u}_h) = 0 \quad (1)$$

$$\frac{\partial(\alpha_h \rho_h \vec{u}_h)}{\partial t} + \nabla \cdot (\alpha_h \rho_h \vec{u}_h \vec{u}_h) = -\nabla \cdot (\alpha_h \tau_h) - \alpha_h \nabla P + \alpha_h \rho_h \vec{g} + F_h \quad (2)$$

where h denotes the phase (the liquid steel: $h = l$, the argon gas: $h = g$), α is the volume fraction, ρ is the density, kg/m^3 , t is the time, s , \vec{u} is the velocity, m/s . The terms on the right-hand side of Equation (2) are shear stress, pressure gradient force, gravity and the interaction force between the liquid and gas phase, N/m^3 .

The stress term of h phase can be described as follows:

$$\tau_h = -\mu_{eff,h} \left(\nabla \vec{u}_h + (\nabla \vec{u}_h)^T - \frac{2}{3} I (\nabla \cdot \vec{u}_h) \right) \quad (3)$$

where $\mu_{eff,h}$ is the effective viscosity, Pa s . The effective viscosity of the liquid phase consists of three contributions:

$$\mu_{eff,l} = \mu_{L,l} + \mu_{T,l} + \mu_{BI,l} \quad (4)$$

where $\mu_{L,l}$, $\mu_{T,l}$, $\mu_{BI,l}$ are the molecular viscosity, turbulence viscosity and an extra term due to bubble-induced turbulence, respectively.

The turbulence induced by the movement of bubbles is calculated using the model proposed by Sato et al. [22], and it is expressed as:

$$\mu_{BI,l} = \rho_l C_{BI,l} \alpha_g d_B \left| \vec{u}_g - \vec{u}_l \right| \quad (5)$$

where $C_{BI,l}$ is the coefficient and equals 0.6, and d_B is the bubble diameter, m .

The calculation of the effective gas viscosity is based on the effective liquid viscosity proposed by Jakobsen et al. [23].

$$\mu_{eff,g} = \frac{\rho_g}{\rho_l} \mu_{eff,l} \quad (6)$$

The realizable k - ε turbulence model is employed in the current model. Compared with the standard k - ε turbulence model, this turbulence model can better predict the spreading rate of jets in the slab mold with a high turbulent Reynolds number [24], which is highly

related to this work. The turbulence viscosity ($\mu_{T,l}$) is calculated from the turbulent kinetic energy k and dissipation rate (ε) as follows:

$$\mu_{T,l} = \rho_l C_{\mu,T} \frac{k^2}{\varepsilon} \quad (7)$$

The turbulent kinetic energy and the dissipation rate are listed as follows:

$$\frac{\partial}{\partial t}(\alpha_l \rho_l k) + \nabla \cdot (\alpha_l \rho_l \vec{u}_l k) = -\nabla \cdot \left(\alpha_l \frac{\mu_{T,l}}{\sigma_k} \nabla k \right) + \alpha_l (G_k - \rho_l \varepsilon) \quad (8)$$

$$\frac{\partial}{\partial t}(\alpha_l \rho_l \varepsilon) + \nabla \cdot (\alpha_l \rho_l \vec{u}_l \varepsilon) = -\nabla \cdot \left(\alpha_l \frac{\mu_{T,l}}{\sigma_\varepsilon} \nabla \varepsilon \right) + \alpha_l \rho_l (C_{1\varepsilon} S \varepsilon - C_{2\varepsilon} \frac{\varepsilon^2}{k + \sqrt{\nu \varepsilon}}) \quad (9)$$

where G_k is the generation of turbulence kinetic energy, m^2/s^2 ; S is the modulus of the mean rate of strain tensor. Model constants: $C_{1\varepsilon} = 1.44$, $C_{2\varepsilon} = 1.9$, $\sigma_k = 1.00$, $\sigma_\varepsilon = 1.2$.

2.2.2. Interaction Force Model

The interaction force \vec{F}_h is as follows:

$$\vec{F}_h = \vec{F}_D + \vec{F}_L + \vec{F}_{VM} + \vec{F}_{TD} + \vec{F}_{WL} \quad (10)$$

where \vec{F}_D is the drag force; \vec{F}_L is the lift force; \vec{F}_{VM} is the virtual mass force; \vec{F}_{TD} is the turbulent dispersion force; \vec{F}_{WL} is the wall lubrication force. The detailed description for these forces can be seen in the Ref [25].

2.2.3. Population Balance Model (PBM)

The population balance model is used to describe the bubble breakage and coalescence. Compared with the traditional Euler–Euler model, the PBM can describe the bubble breakage and coalescence and then predict the bubble size distribution, frequency, etc. The description can be written as follows:

$$\frac{\partial}{\partial t} n_i + \nabla \cdot (\vec{u}_g n_i) = B_i^B - D_i^B + B_i^C - D_i^C \quad (11)$$

where n_i is the number density of group- i bubbles, $1/m^3$; \vec{u}_i is the velocity of group- i bubbles, m/s ; B_i^B and D_i^B are the birth and death rate of group- i bubbles due to bubble breakage, $1/(m^3 \cdot s)$, B_i^C and D_i^C are the birth and death rate of group- i bubbles due to bubble coalescence, $1/(m^3 \cdot s)$. In this study, the birth rate and the disappearance rate of bubble breakage are calculated using the Luo and Svendsen model [26]; the birth rate and the disappearance rate of bubble coalescence are calculated using the Luo model [27].

2.3. Geometric Model and Boundary Conditions

2.3.1. Geometric Model and Mesh

The geometric model of simulation is presented in Figure 1a, including the tundish, stopper rod, TUN, SEN and mold. The section of the mold is $1650 \text{ mm} \times 230 \text{ mm}$ and the effective length is 800 mm . In order to ensure that the flow fully develops, the length of the calculation domain is extended to 3000 mm . The calculation domain is divided into 1.7 million finite volumes using a hexahedral structure grid, as shown in Figure 1b. The skewness of the grid is less than 0.8 and the comprehensive grid quality is greater than 0.5, which meet the demands of numerical simulation. Meanwhile, the grid-independent verification is carried out. Table 1 shows the geometric parameters and physical properties for the numerical simulation.

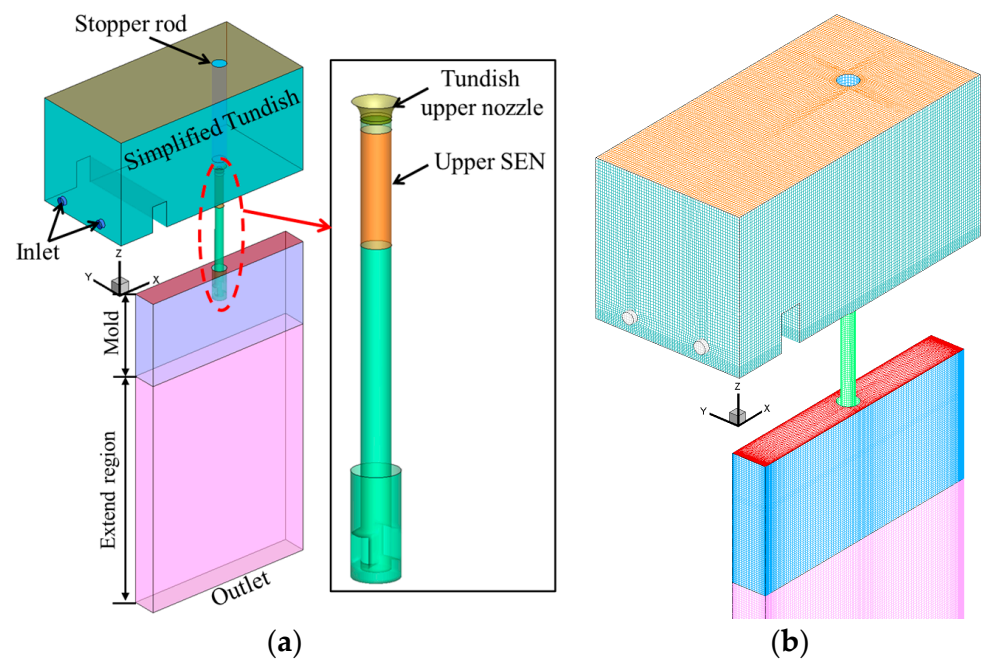


Figure 1. (a) Geometric model diagram (b) Model mesh.

Table 1. Geometric parameters and physical properties in numerical simulation.

Parameter	Value
Mold size (mm × mm)	1650 × 230
Size of SEN port (mm × mm)	60 × 80
Inner diameter of SEN (mm)	80
Outer diameter of SEN (mm)	130
Inclination angle (°)	15
Submerged entry depth (mm)	165
Steel density (kg/m ³)	7000
Steel viscosity (Pa·s)	0.0065
Argon gas density (kg/m ³)	0.27 at 1803 K
Argon gas viscosity (Pa·s)	8.1×10^{-5} at 1803 K

2.3.2. Boundary Conditions

The inlet of liquid steel and argon is defined as the mass inlet, the value of which was determined based on the casting speed and gas flow rate, respectively. Table 2 shows the transformed mass flow rate under different process parameters. A pressure outlet boundary condition at the bottom of the calculation domain was adopted. The top surfaces of the mold and tundish were set as the degassing boundary condition, which means that only the gas phase could escape from it. The no-slip boundary condition was adopted at the other walls of the calculation domain. Figure 2 shows the schematic of two types of argon injection modes in the current work, namely the argon injection from the stopper rod and upper SEN (Case 1) and the argon injection from the stopper rod and tundish upper nozzle (Case 2).

2.4. Numerical Details

In the current study, the gas–liquid two-phase flow mathematical model was considered in the continuous casting mold with argon blowing. The model was solved using ANSYS-FLUENT 18.2 (ANSYS Inc., Pittsburgh, PA, USA). The Euler–Euler model was applied and the argon bubble was treated as a continuous phase. In order to investigate the bubble breakage and coalescence behavior, the PBM was adopted, where the bubble size ranged from 0 mm to 6 mm with 11 size groups [21]. The initial bubble diameter entering

the calculation domain was 2 mm. The Phase Coupled SIMPLE scheme was utilized for the pressure–velocity coupling. For high accuracy, the second-order upwind scheme was adopted for discretizing the momentum, turbulent kinetic energy, turbulent dissipation rate and bubble size groups. The convergence residual was set to 0.001 for all variables. The time step was set to 0.001 s and the total calculation time was 100 s.

Table 2. Process parameters in this study.

Parameter	Value (SI)	Mass Flow Rate (kg/s)
Casting speed	0.7, 0.9, 1.1, 1.3	15.45, 19.87, 24.28, 28.7
Flow rate of argon injection at the Stopper rod	4	1.189×10^{-4}
Flow rate of argon injection at the SEN	0, 4, 5, 7	0, 1.189×10^{-4} , 1.486×10^{-4} , 2.08×10^{-4}
Flow rate of argon injection at the TUN	0, 4, 5, 7	0, 1.189×10^{-4} , 1.486×10^{-4} , 2.08×10^{-4}

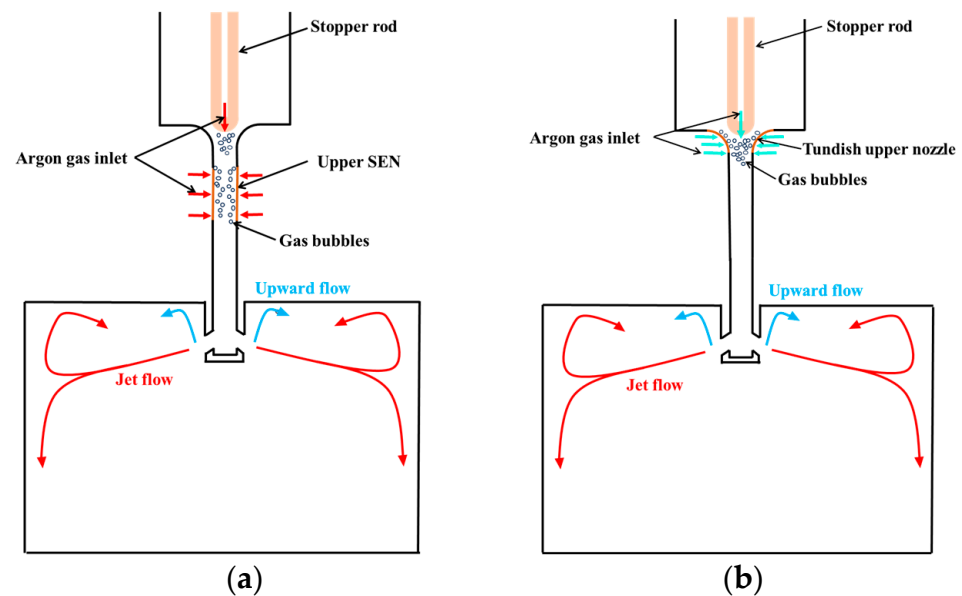


Figure 2. Schematics of argon injection modes (a) Case 1 (b) Case 2.

3. Modeling Validation

In order to validate the mathematical model, a 1:2 scale water model was established based on the similarity principle. Water was circulated through pipes and a pump to a buffer cuboid to simplify the tundish, and argon gas was injected into the SEN through the stopper rod and a circumferential inlet chamber which was made from dispersed mullite porous brick. As the water and argon flow reached a steady state, an image of bubble distribution within the mold was taken by using a high-speed camera. Figure 3 shows the bubble distribution within the mold at the casting speed of 0.63 m/min and argon flow rate of 0.638 L/min at the SEN. It can be seen that most of the bubbles floated near the SEN, especially the large bubbles, while the small bubbles moved along with the jet flow to the narrow face because of the effect of buoyancy, which is consistent with the flow characteristics calculated by Zhang [21] and Yang [28]. The bubble diameters within the mold obtained by the current model are shown in Figure 3b, which indicates that both the distribution and penetrating depth of argon bubbles agree well with the experiment.

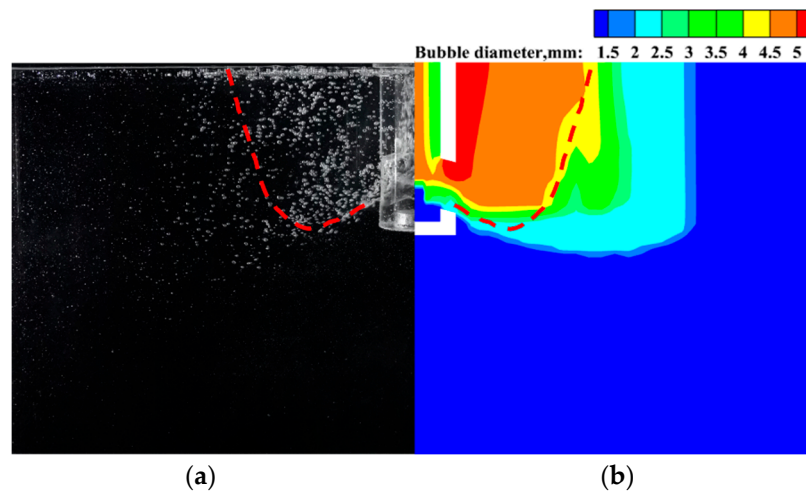


Figure 3. (a) Bubble distribution results of water model experiment (b) Bubble distribution results of numerical simulation.

4. Results and Discussion

4.1. Effect of Argon Injection Mode and Argon Flow Rate on the Bubble Distribution and Flow Field

A. Analysis of Bubble Distribution within the Mold

Figure 4 shows the effect of the argon injection mode and argon flow rate on the bubble size distribution inside the mold under the casting speed of 1.1 m/min. All of the cases show that bubbles of a large size can float up near the SEN, and the floating region is far away from the SEN with decreasing bubble size. It can be seen that the bubble size distribution in the mold of Case 1 is similar to that of Case 2 under the same argon flow rate. As the bubbles enter the mold, large bubbles with high buoyancy easily float near the SEN and then escape from the mold’s top surface; the maximum bubble diameter was 4.8 mm. Meanwhile, through comparison of the argon flow rate (Figure 4a,c), the concentration of argon bubbles in the upper region of the mold increased with increasing argon flow rate. The possible reason is that the number of argon bubbles entering the mold increases with increasing argon flow rate, which can enhance the coalescence rate of bubbles within the mold.

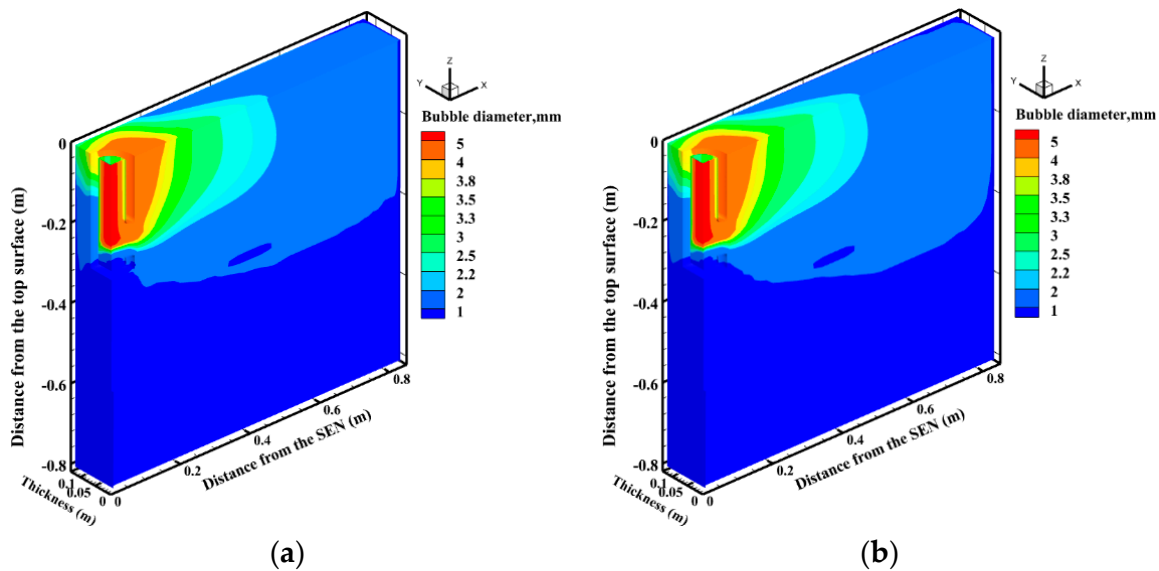


Figure 4. Cont.

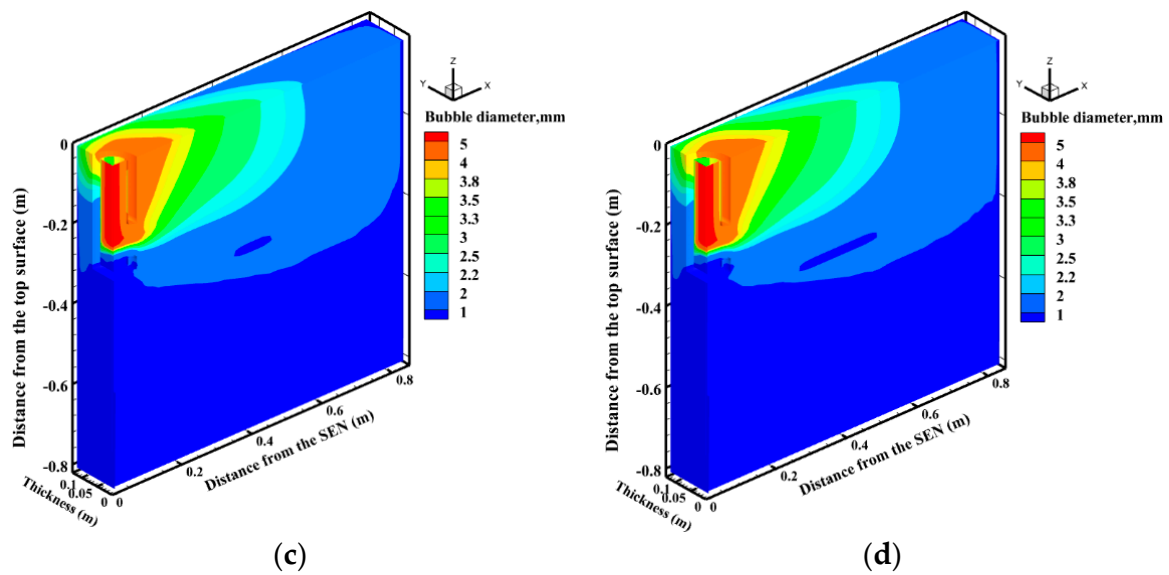


Figure 4. Argon bubble size distribution inside the mold under different argon injection modes and argon flow rates (a) Case 1, 8 L/min; (b) Case 2, 8 L/min; (c) Case 1, 11 L/min; (d) Case 2, 11 L/min.

To further discuss the influence of argon injection mode on bubble distribution, Figure 5 shows the bubble distribution frequency and average bubble diameter in the upper recirculation zone ($Z > -165$ mm) of the mold under the casting speed of 1.1 m/min. As shown in Figure 5a, most bubbles are concentrated at the size of 1~2 mm for both argon injection modes, and are over 80%. With the increase in bubble size, the frequency of bubble distribution decreases, and only 1% of bubbles with the diameter of 4.5~5 mm exist in the upper region of the mold, which also indicates that as argon bubbles enter the mold, the breakage phenomena are predominant. In addition, the distribution regularity for both cases is similar.

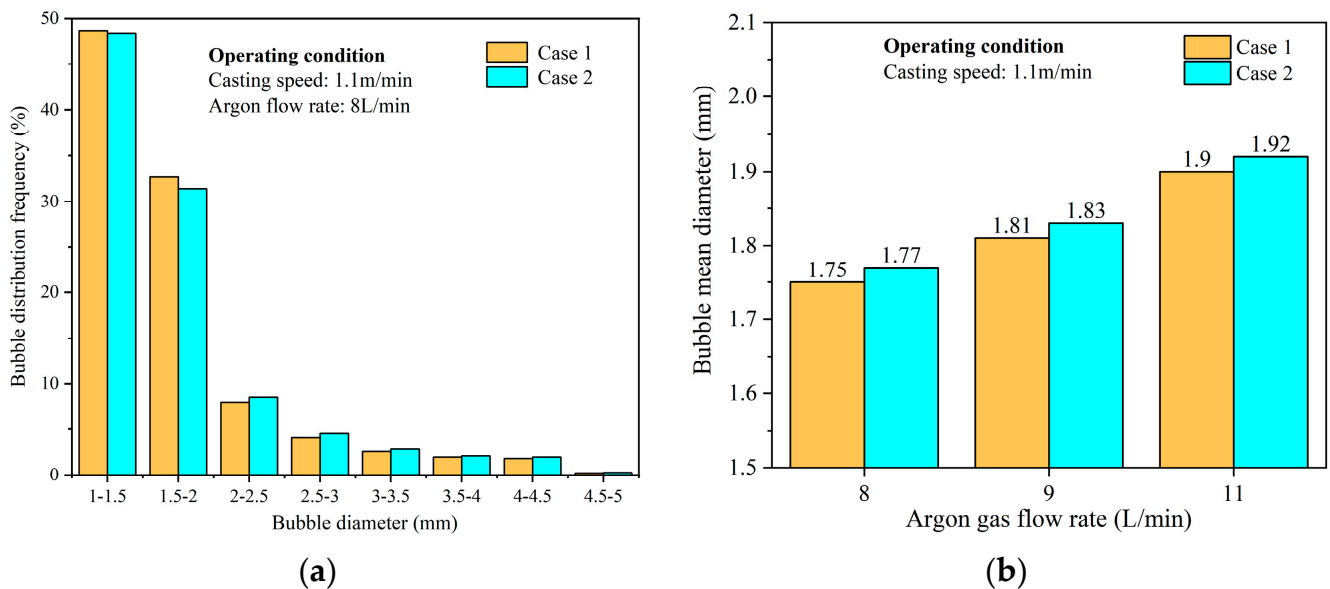


Figure 5. Argon bubble size distribution in the upper recirculation zone of mold with different argon injection modes (a) Bubble distribution frequency; (b) Bubble average diameter.

The average bubble diameter under different argon injection modes and argon flow rates is shown in Figure 5b. It can be seen that the bubble diameter increases with increasing argon flow rate, as the argon flow rate for Case 1 increases from 8 L/min to 11 L/min; the average bubble diameters increase from 1.75 mm to 1.9 mm, the high argon flow rate increases the number of bubbles entering the mold, and then increases the probability of bubble coalescence. Meanwhile, another phenomenon can be seen where the bubble diameter also changes insignificantly under different argon injection modes but under the same argon flow rate.

Figure 6 shows the number density of bubbles inside the mold under different argon injection modes. The number density of bubbles decreases significantly with increasing bubble size, indicating that the bubbles mainly break up after entering the mold, because of the strong shear force of the jet flow. Meanwhile, compared with Case 1, it can be seen that the number density of bubbles for Case 2 is larger, which illustrates that the number of bubbles in the mold is greater in Case 2. This may increase the probability of bubbles being captured by the solidified shell and cause surface defects such as slivers and pencil pipe defects [29,30].

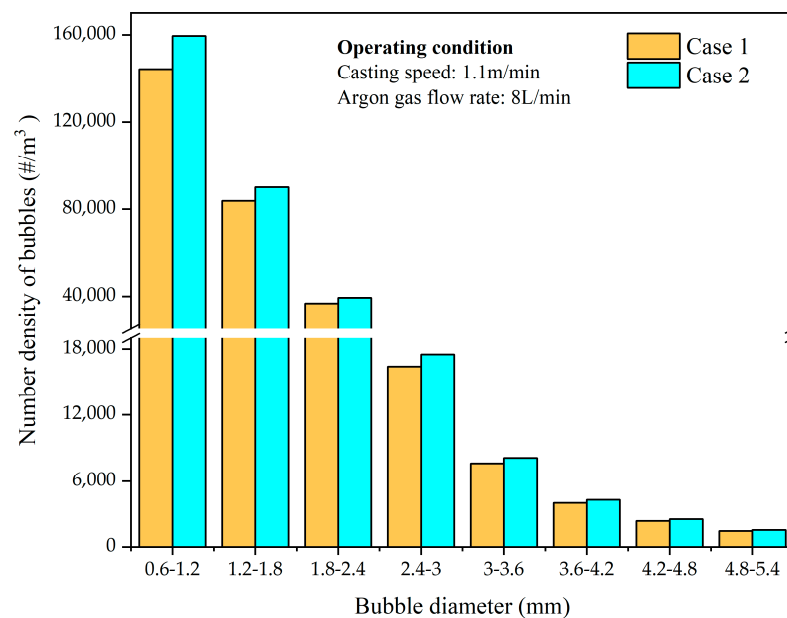


Figure 6. The number density of bubbles inside the mold under different argon injection modes.

B. Analysis of Liquid Steel Flow Field in the Mold

In continuous casting, the argon injection can directly influence the flow pattern within the mold. Figure 7 shows the velocity contour at the center longitudinal plane under different argon injection modes at the casting speed of 1.1 m/min. Under the condition of only argon injection at the stopper rod (Figure 7a), the argon flow rate is relatively low such that the flow pattern is still a classical 'double-roll' pattern, and there exists a small part of upward flow near the SEN. Under the condition of argon injection at the SEN and TUN (Figure 7b,c) in combination with the argon injection mode, the flow pattern within the mold changes significantly, especially in the upper region of the mold; the upper recirculation flow disappears and the flow pattern changes to complex flow, and the floating bubbles carry the liquid steel to move upward to the top surface. The flow pattern is similar under the different argon injection modes which results from the similar bubble distribution and bubble diameter (Figure 5).

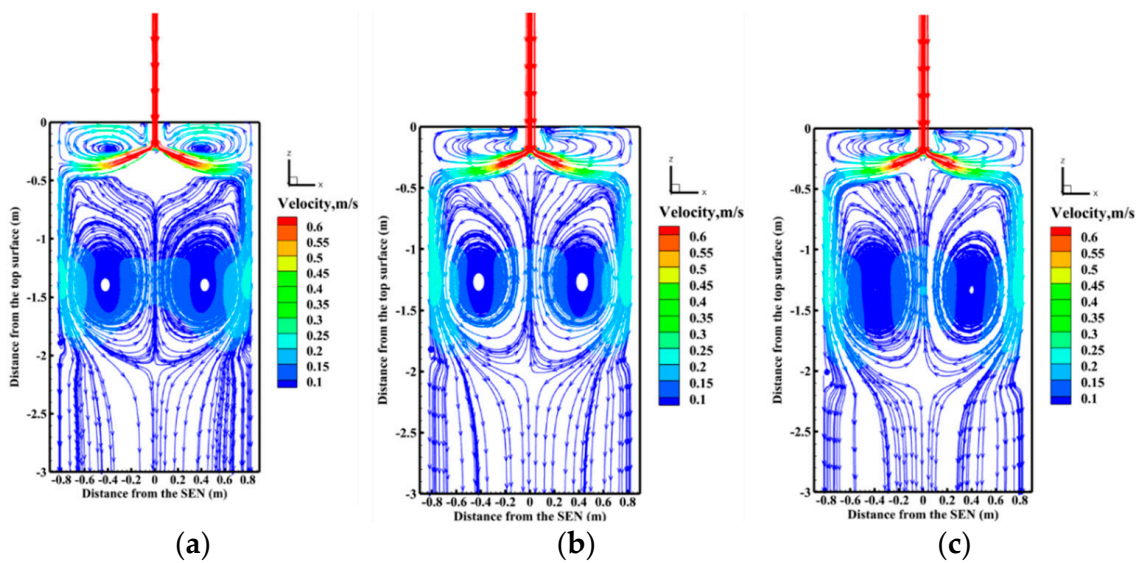


Figure 7. Flow field distribution of liquid steel in mold with different argon injection modes (a) Only the stopper rod injection, 4 L/min; (b) Case 1, 8 L/min; (c) Case 2, 8 L/min.

Figure 8 shows the effect of the argon injection mode on the velocity distribution of liquid steel at the centerline of the mold’s top surface under the casting speed of 1.1 m/min. When there is only stopper rod injection under the argon flow rate of 4 L/min, the velocity peak is at 1/4 of the width of the mold, and the maximum velocity is 0.3 m/s. With an increase in the argon flow rate, the speed increases near the SEN since the effect of bubbles on the jets becomes weak, and it decreases at a quarter of the mold’s width. When the argon flow rate is 11 L/min, the velocity peak is near the SEN and the maximum velocity exceeds 0.1 m/s, which illustrates that the change of flow pattern has a significant effect on the velocities of the top surface in the mold. In addition, both cases have similar velocity distributions.

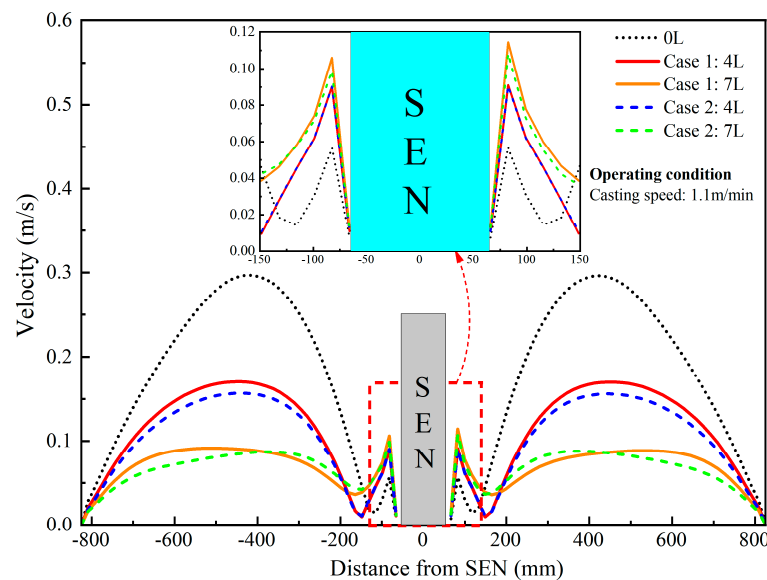


Figure 8. Velocity at the centerline of mold’s top surface under different argon injection modes.

C. Analysis of Level Fluctuation at the Steel–Slag Interface

Flow across the top face can influence the surface-level profile and its fluctuations. In order to evaluate the level fluctuation at the steel–slag interface, the level height is

calculated by converting the surface pressure distribution according to the simplified potential energy balance [31], which is described as follows:

$$H = \frac{P - P_{mean}}{(\rho_{steel} - \rho_{slag})g} \quad (12)$$

where P is the pressure at the top surface, Pa, P_{mean} is the average pressure across the entire top surface, Pa, and ρ_{steel} and ρ_{slag} are the density of liquid steel and slag, kg/m^3 .

Figure 9 shows the profile of level fluctuation under different argon injection modes at the casting speed of 1.1 m/min. As shown in Figure 9a, with only stopper rod injection and an argon flow rate of 4 L/min, the large level fluctuation mainly occurs at the narrow face and near the SEN owing to the effect of jet flow and upward flow caused by argon bubbles. Under the condition of combined argon injection modes with argon flow rates of 8 L/min (Figure 9b,c), the level fluctuation near the SEN increases obviously, and the level fluctuation at the narrow surface decreases. Meanwhile, the level fluctuation is similar under different argon injection modes for the same argon flow rate.

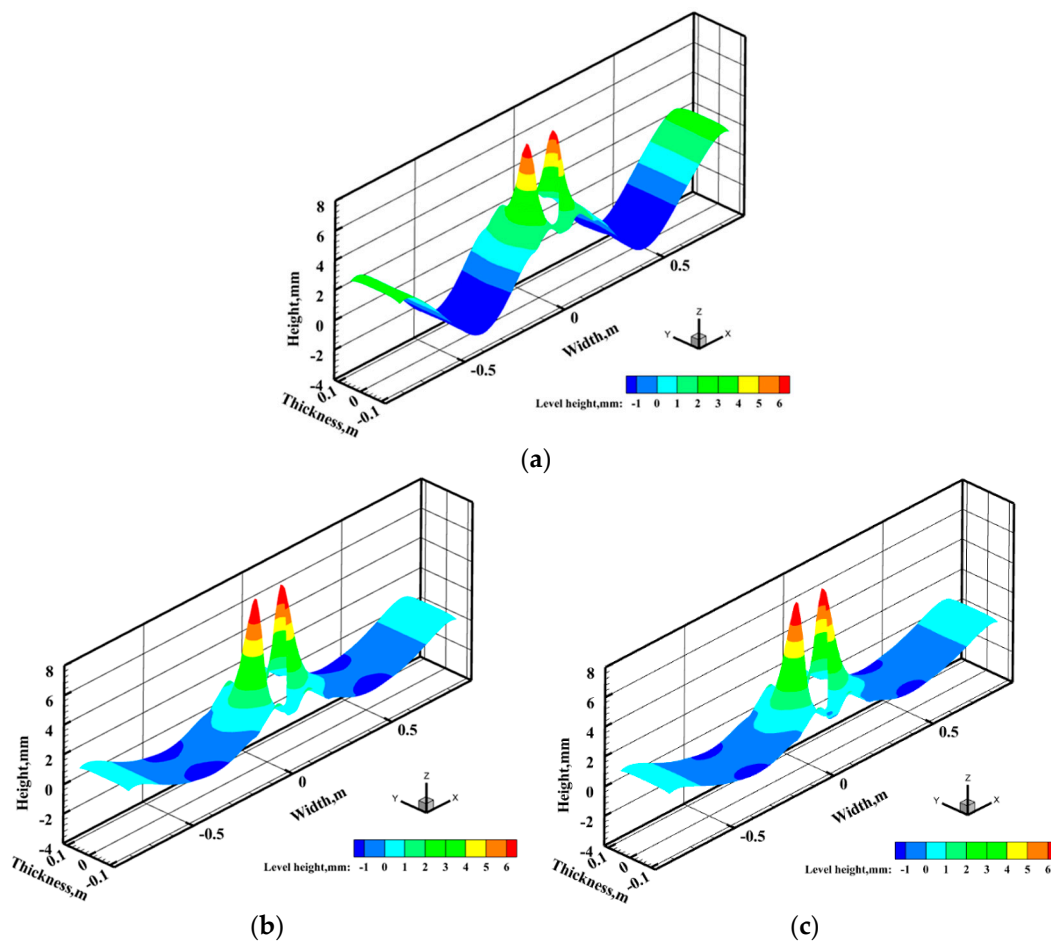


Figure 9. Level fluctuation at the top surface of mold under different argon injection modes and argon flow rates (a) Only the stopper rod injection, 4 L/min; (b) Case 1, 8 L/min; (c) Case 2, 8 L/min.

Figure 10 shows the level height at the centerline of the mold's top surface under different injection modes. It can be seen that by applying combined argon injection, the level fluctuation near the narrow face decreases significantly, while the level height near the SEN increases. The value is greater than 7 mm near the SEN, which may increase the risk of slag entrapment and the formation of slag eye. Furthermore, the level fluctuation

changes insignificantly under the different argon injection modes due to the similar bubble size and velocity of liquid steel.

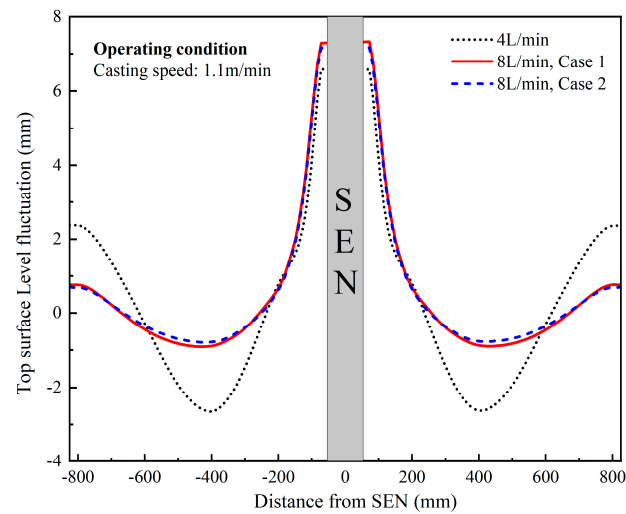


Figure 10. Level fluctuation at the centerline of mold's top surface under different argon injection modes.

From Figures 4–10, under the condition of the same casting speed and argon flow rate, the different argon injection modes have similar bubble distributions, flow patterns of liquid steel and level fluctuations at the steel–slag interface. However, the number of bubbles in Case 1 is less than that of Case 2, which could reduce the probability of entrapping by solidified shell. Thus, the argon injection Case 1 was applied in the subsequent analysis.

4.2. Effect of Casting Speed on the Bubble Distribution and Flow Field

A. Analysis of Bubble Distribution in the Mold

Figure 11 shows the bubble size distribution inside the mold under different casting speeds with an 8 L/min argon flow rate. It can be seen that the bubble size decreases with increasing casting speed, which illustrates that the breakup rate of argon bubbles increases with increasing casting speed. When the casting speed is 0.7 m/min (Figure 11a), the kinetic energy of the liquid steel is insufficient to break up the large bubbles. When the casting speed exceeds 1.1 m/min (Figure 11c,d), the strong turbulence energy and shear force of the jet flow make the large bubbles break up, and the smaller bubbles can move with the jet flow to the deep mold cavity at the higher casting speed.

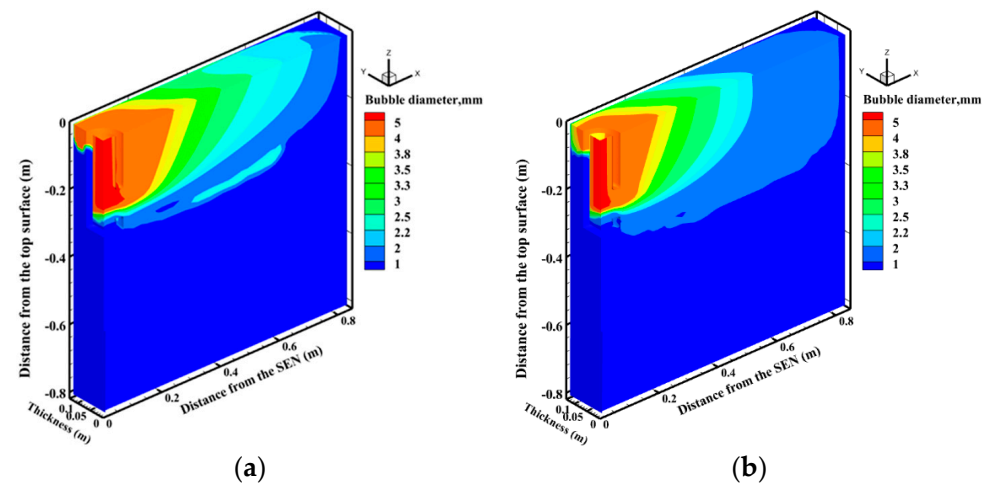


Figure 11. Cont.

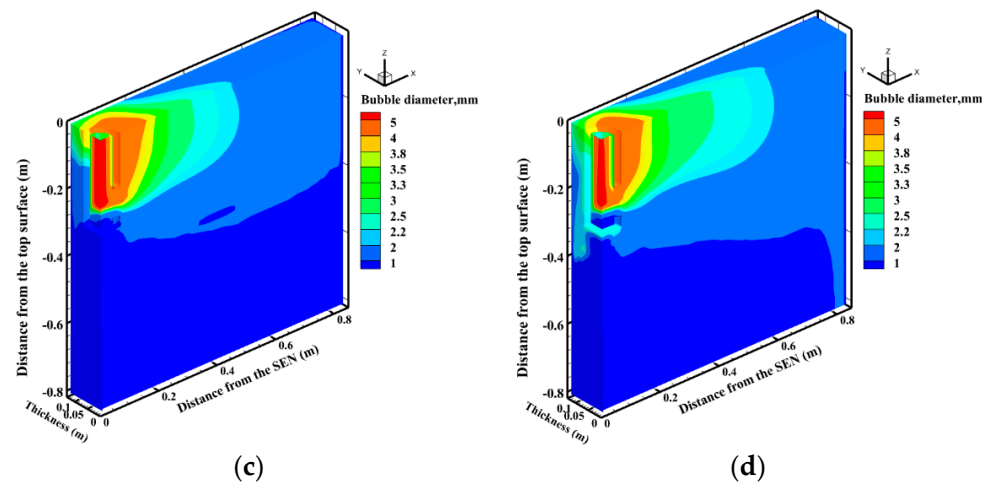


Figure 11. Argon bubble size distribution inside the mold under different casting speeds (a) 0.7 m/min; (b) 0.9 m/min; (c) 1.1 m/min; (d) 1.3 m/min.

In order to analyze the bubble behavior quantitatively, Figure 12 shows the bubble distribution frequency and average bubble diameter under different casting speeds. It can be seen that for a low casting speed, bubbles mainly concentrate at the size of 2~3 mm. Owing to the small turbulence energy and shear force, bubbles easily aggregate with the mold (initial bubble diameter: 2 mm). With the increase in casting speed, the ratio of small bubble diameter increases, and the bubble size in the range of 1~2 mm increases to 83% as the casting speed increases to 1.3 m/min. The breakage behavior is predominant under a high casting speed, and the corresponding average bubble diameter is shown in Figure 12b. The bubble diameter decreases with the increase in casting speed, as a large casting speed increases the probability of bubble breakup, and causes a decrease in bubble diameter within the mold. As the casting speed changes to 1.3 m/min, the average bubble diameter decreases to 1.73 mm.

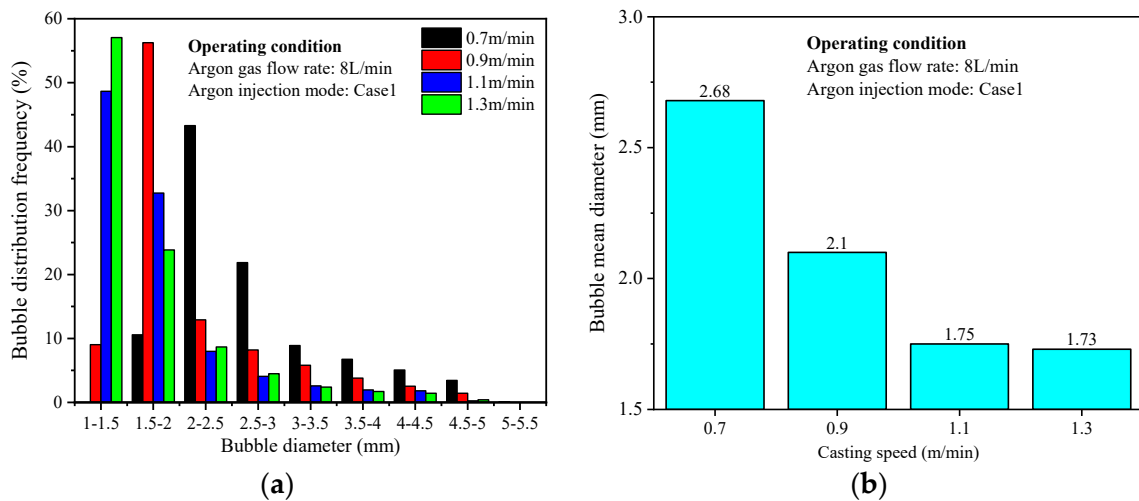


Figure 12. Argon bubble size distribution in the upper recirculation zone of mold with different casting speeds (a) Bubble distribution frequency; (b) Bubble average diameter.

Figure 13 shows the number density of bubbles inside the mold under different casting speeds. The number density of bubbles increases with increasing casting speed under the bubble diameter of 0.6~1.2 mm, indicating that the number of small bubbles increases with an increase in the casting speed since the strong kinetic energy of liquid steel leads to the larger breakup rate of bubbles. The number density of bubbles decreases with increasing

casting speed for 3.6~5.4 mm bubbles, which illustrates that a high casting speed promotes the breakup of large bubbles.

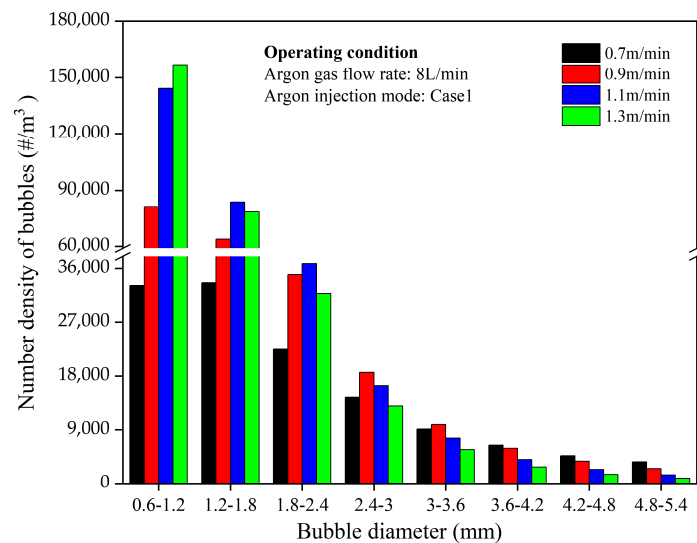


Figure 13. The number density of bubbles inside the mold under different casting speeds.

B. Analysis of Liquid Steel Flow Field in the Mold

Figure 14 shows the velocity contour at the center longitudinal plane under different casting speeds under the argon flow rate of 8 L/min. In Figure 14a, when the casting speed is 0.7 m/min, most of the stream moves up toward the top surface after leaving the port of the SEN due to the buoyancy of argon bubbles, which illustrates that the flow pattern is single-roll flow. The main reason is that the kinetic energy of the liquid steel is weak and is insufficient to break up large bubbles, while the large bubbles have a great effect on the jet flow. As the casting speed increases, the jet flow velocity is obviously enhanced, and the large bubbles break up into smaller ones. When the casting speed exceeds 1.1 m/min as shown in Figure 14c,d, the upper recirculation flow appears, and the flow pattern becomes closer to that of the double-roll flow.

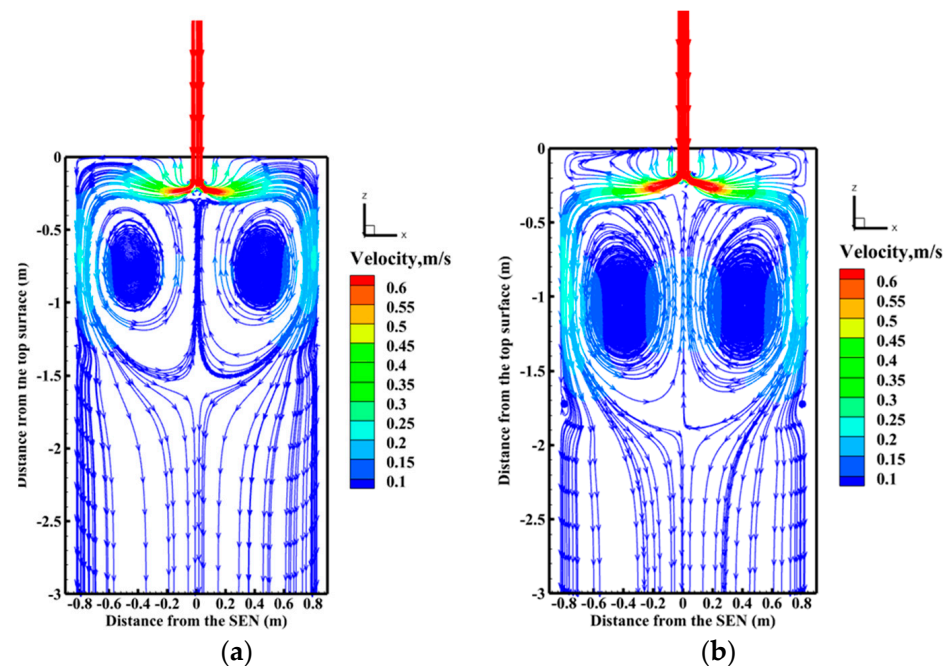


Figure 14. Cont.

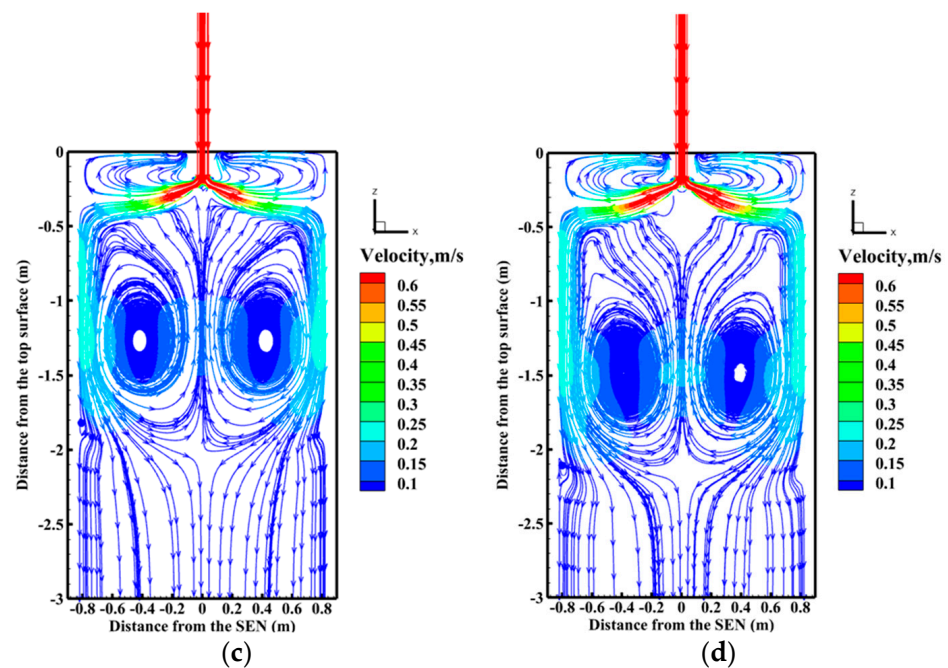


Figure 14. Flow field distribution of liquid steel in mold under different casting speeds (a) 0.7 m/min (b) 0.9 m/min (c) 1.1 m/min (d) 1.3 m/min.

Figure 15 shows the effect of casting speed on the velocity distribution of liquid steel at the centerline of the mold's top surface under the argon flow rate of 8 L/min. When the casting speed is 0.7 m/min, the flow pattern is single-roll flow, the velocity peak is near the SEN, and the value exceeds 0.11 m/s. With an increase in the casting speed, the flow in the upper recirculation zone is intensified, and the flow pattern of liquid steel transforms to double-roll flow. When the casting speed exceeds 1.1 m/min, the velocity peak is near the 1/4 width of the mold, and the maximum speed exceeds 0.23 m/s with the casting speed of 1.3 m/min, which illustrates that the casting speed can remarkably strengthen the flow at the top surface of the mold.

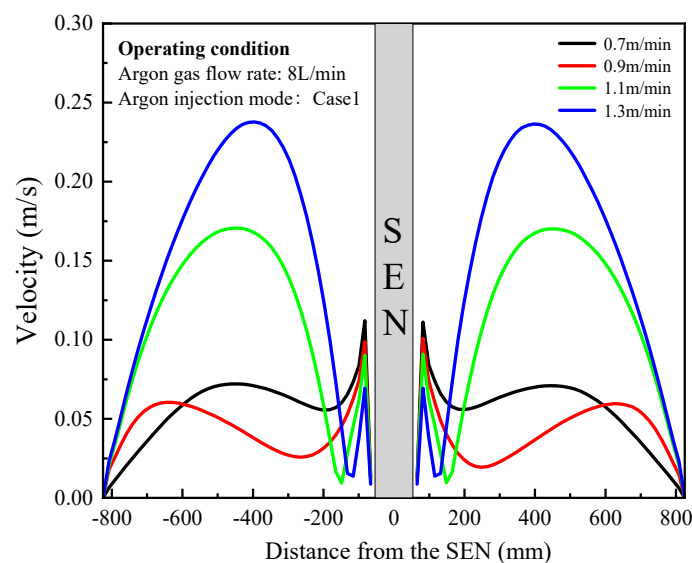


Figure 15. Velocity at the centerline of mold's top surface under different casting speeds.

C. Analysis of Level Fluctuation at the Steel–Slag Interface

Figure 16 shows the profile of level fluctuation under different casting speeds under the argon flow rate of 8 L/min. When the casting is 0.7 m/min with the flow pattern of

single-roll flow, as shown in Figure 16a, the level near the SEN is obviously large, and other areas are relatively flat. The main reason is that the number of large bubbles is greater, and most of the liquid steel moves toward the top surface near the SEN due to the effect of the buoyancy of large bubbles under low casting speed. When the casting speed is 1.1 and 1.3 m/min (Figure 16c,d), the increase in casting speed strengthens the upper recirculation flow, and the effect of bubble buoyancy on jet flow becomes weak, leading to the level fluctuation near the SEN decreasing and the level fluctuation at the narrow surface increasing.

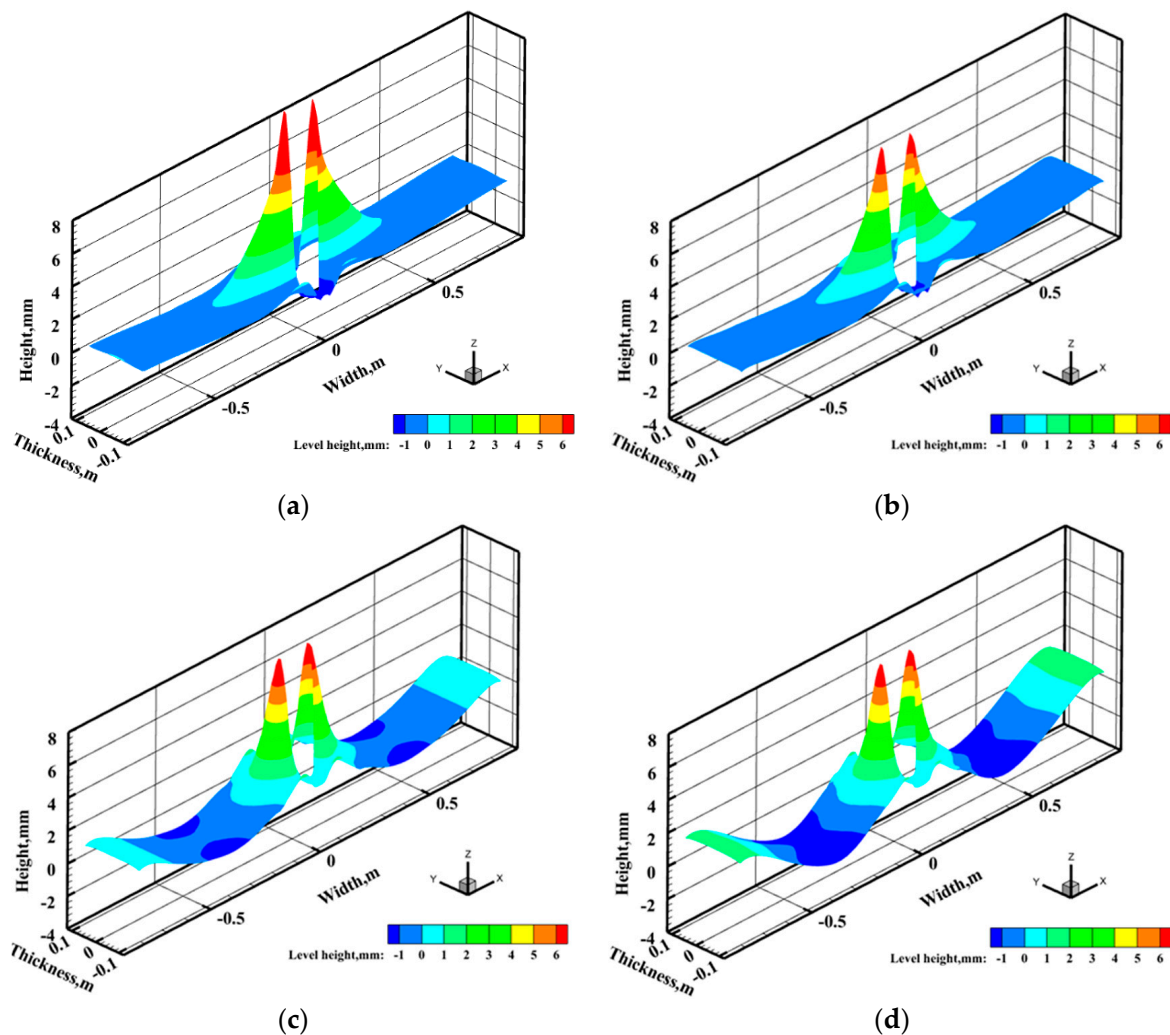


Figure 16. Level fluctuation at the mold's top surface under different casting speeds (a) 0.7 m/min (b) 0.9 m/min (c) 1.1 m/min (d) 1.3 m/min.

Figure 17 illustrates the level height at the centerline of the mold's top surface under different casting speeds with the argon flow rate of 8 L/min. When the casting speed is 0.7 m/min and 0.9 m/min, the top surface level gradually decreases from the SEN to the narrow surface. The liquid level fluctuation near the SEN exceeds 8 mm at the casting speed of 0.7 m/min, which may cause the liquid slag to be entrapped in the liquid steel in the area of the SEN. When the casting speed increases to 1.1 m/min and 1.3 m/min, the liquid level decreases first then increases from the SEN to the narrow surface. The main reason is that the flow pattern tends to be transformed into double-roll flow and the increase in the casting speed intensifies the impact of the upper recirculation flow on the meniscus.

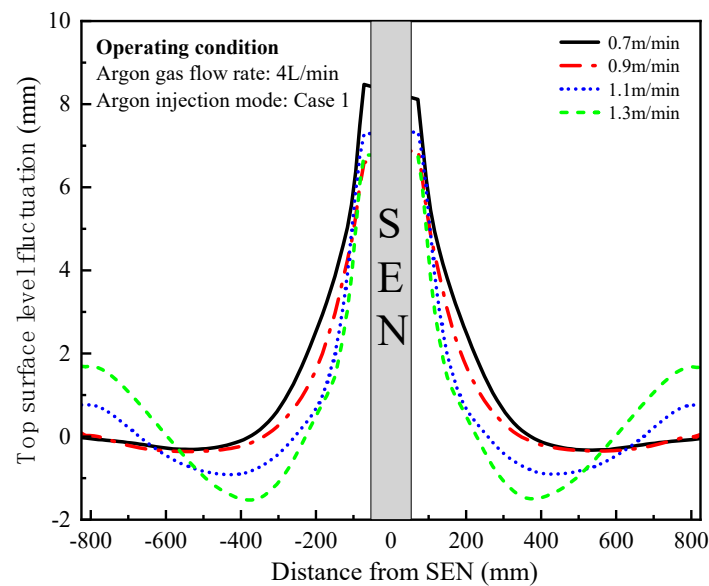


Figure 17. Level fluctuation at the centerline of mold's top surface under different casting speeds.

5. Conclusions

In this work, a three-dimensional mathematical model is established to investigate the liquid steel flow, bubble distribution characteristic under different argon injection modes, argon flow rates and casting speeds in a slab mold. The main conclusions are summarized as follows:

- (1) The numerical simulation results show that large bubbles float near the SEN and small bubbles move along with the jet flow to the narrow face. This is consistent with the results of the water model experiment.
- (2) Under the condition with the same casting speed and argon flow rate, the different argon injection modes have similar bubble distributions, flow patterns of liquid steel and level fluctuations at the steel–slag interface. However, the coalescence rate of bubbles is higher and the number of bubbles is greater under argon injection from the stopper rod and tundish upper nozzle, which make the bubbles easy to be captured by the solidified shell.
- (3) The increase in argon flow rate enhances the bubble coalescence rate and the velocity near the nozzle. When the argon flow rate exceeds 4 L/min, the flow pattern of liquid steel changes from double-roll flow to complex flow at the casting speed of 1.1 m/min, aggravating the level fluctuation of the top surface near the SEN.
- (4) The speed of the liquid steel at the 1/4 width at the top surface of the mold and the breakup rate of bubbles inside the mold increase with increasing casting speed. A high casting speed is conducive to the formation of double-roll flow, and the liquid level at the narrow face of the top surface increases.

Author Contributions: Conceptualization, H.L. and Z.L.; methodology, H.L. and J.S.; software, Q.C.; validation, Z.H.; formal analysis, Z.H.; investigation, Y.Z. and C.C.; writing—original draft preparation, Z.H.; writing—review and editing, Q.C. and J.S.; supervision, Z.L. and J.S.; project administration, J.S.; funding acquisition, Z.L. and H.L. All authors have read and agreed to the published version of the manuscript.

Funding: This work was financially supported by National Science Foundation of China (NO. 52074181, 52304353), the fellowship of China Postdoctoral Science Foundation (2023TQ0208), Independent Research Project of the State Key Laboratory of Advanced Special Steel, Shanghai University (SKLASS-2023-Z03) and the Science and Technology Commission of Shanghai Municipality (No.19DZ2270200) and Shanghai Technical Service Center of Science and Engineering Computing, Shanghai University.

Data Availability Statement: The data presented in this study are available in this paper.

Conflicts of Interest: The authors declare no conflict of interest.

References

1. Yang, H.; Olia, H.; Thomas, B.G. Modeling Air Aspiration in Steel Continuous Casting Slide-Gate Nozzles. *Metals* **2021**, *11*, 116. [[CrossRef](#)]
2. Thomas, B.G.; Huang, X.; Sussman, R. Simulation of argon gas flow effects in a continuous slab caster. *Metall. Mater. Trans. B* **1994**, *25*, 527–547. [[CrossRef](#)]
3. Bai, H.; Thomas, B.G. Effects of clogging, argon injection, and continuous casting conditions on flow and air aspiration in submerged entry nozzles. *Metall. Mater. Trans. B* **2001**, *32*, 707–722. [[CrossRef](#)]
4. Cho, J.; Lee, H. Cold model study on inclusion removal from liquid steel using fine gas bubbles. *ISIJ Int.* **2001**, *41*, 151–157. [[CrossRef](#)]
5. Yang, H.; He, P.; Zhai, Y. Removal behavior of inclusions in molten steel by bubble wake flow based on water model experiment. *ISIJ Int.* **2014**, *54*, 578–581. [[CrossRef](#)]
6. Yang, W.; He, P.; Chang, L.; Li, T.; Bai, X.; Luo, Z.; Zhao, N.; Liu, Q. Numerical Analysis of Slag–Steel–Air Four-Phase Flow in Steel Continuous Casting Model Using CFD-DBM-VOF Model. *Metals* **2023**, *13*, 1943. [[CrossRef](#)]
7. Bai, H.; Thomas, B.G. Bubble formation during horizontal gas injection into downward-flowing liquid. *Metall. Mater. Trans. B* **2001**, *32*, 1143–1159. [[CrossRef](#)]
8. Wu, Y.; Liu, Z.; Wang, F.; Li, B.; Gan, Y. Experimental investigation of trajectories, velocities and size distributions of bubbles in a continuous-casting mold. *Powder Technol.* **2021**, *387*, 325–335. [[CrossRef](#)]
9. Cho, S.; Thomas, B.G.; Kim, S. Bubble behavior and size distributions in stopper-rod nozzle and mold during continuous casting of steel slabs. *ISIJ Int.* **2018**, *58*, 1443–1452. [[CrossRef](#)]
10. Vynnycky, M. Applied Mathematical Modelling of Continuous Casting Processes: A Review. *Metals* **2018**, *8*, 928. [[CrossRef](#)]
11. Cho, S.; Thomas, B.G. Electromagnetic forces in continuous casting of steel slabs. *Metals* **2019**, *9*, 471. [[CrossRef](#)]
12. Yang, H.; Vanka, S.P.; Thomas, B.G. Mathematical modeling of multiphase flow in steel continuous casting. *ISIJ Int.* **2019**, *59*, 956–972. [[CrossRef](#)]
13. Liu, Y.; Yang, J.; Huang, F.; Zhu, K.; Liu, F.; Gong, J. Comparison of the Flow Field in a Slab Continuous Casting Mold between the Thicknesses of 180 mm and 250 mm by High Temperature Quantitative Measurement and Numerical Simulation. *Metals* **2021**, *11*, 1886. [[CrossRef](#)]
14. Zhang, T.; Yang, J.; Jiang, P. Measurement of Molten Steel Velocity near the Surface and Modeling for Transient Fluid Flow in the Continuous Casting Mold. *Metals* **2019**, *9*, 36. [[CrossRef](#)]
15. Liu, C.; Luo, Z.; Zhang, T.; Deng, S.; Wang, N.; Zou, Z. Mathematical modeling of multi-sized argon gas bubbles motion and its impact on melt flow in continuous casting mold of steel. *J. Iron Steel Res. Int.* **2014**, *21*, 403–407. [[CrossRef](#)]
16. Chen, W.; Ren, Y.; Zhang, L.; Scheller, P.R. Numerical simulation of steel and argon gas two-phase flow in continuous casting using LES+ VOF+ DPM model. *JOM* **2019**, *71*, 1158–1168. [[CrossRef](#)]
17. Wu, Y.; Liu, Z.; Li, B.; Gan, Y. Numerical simulation of multi-size bubbly flow in a continuous casting mold using population balance model. *Powder Technol.* **2022**, *396*, 224–240. [[CrossRef](#)]
18. Liu, Z.; Li, B.; Qi, F.; Cheung, S. Population balance modeling of polydispersed bubbly flow in continuous casting using average bubble number density approach. *Powder Technol.* **2017**, *319*, 139–147. [[CrossRef](#)]
19. Liu, Z.; Li, L.; Qi, F.; Li, B.; Jiang, M.; Tsukihashi, F. Population balance modeling of polydispersed bubbly flow in continuous-casting using multiple-size-group approach. *Metall. Mater. Trans. B* **2015**, *46*, 406–420. [[CrossRef](#)]
20. Liu, Z.; Qi, F.; Li, B.; Cheung, S. Modeling of bubble behaviors and size distribution in a slab continuous casting mold. *Int. J. Multiph. Flow* **2016**, *79*, 190–201. [[CrossRef](#)]
21. Liu, Z.; Zhang, L.; Zhou, H.; Chen, W. Study on the Spatial Distribution of Argon Bubbles in a Steel Slab Continuous Casting Strand. *Steel Res. Int.* **2022**, *93*, 2100413. [[CrossRef](#)]
22. Sato, Y.; Sekoguchi, K. Liquid velocity distribution in two-phase bubble flow. *Int. J. Multiph. Flow* **1975**, *2*, 79–95. [[CrossRef](#)]
23. Jakobsen, H.A.; Sannæs, B.H.; Grevskott, S.; Svendsen, H.F. Modeling of vertical bubble-driven flows. *Ind. Eng. Chem. Res.* **1997**, *36*, 4052–4074. [[CrossRef](#)]
24. Liu, H.; Yang, C.; Zhang, H.; Zhai, Q.; Gan, Y. Numerical simulation of fluid flow and thermal characteristics of thin slab in the funnel-type molds of two casters. *ISIJ Int.* **2011**, *51*, 392–401. [[CrossRef](#)]
25. Liu, Z.; Li, B. Large-eddy simulation of transient horizontal gas–liquid flow in continuous casting using dynamic subgrid-scale model. *Metall. Mater. Trans. B* **2017**, *48*, 1833–1849. [[CrossRef](#)]
26. Luo, H.; Svendsen, H.F. Theoretical model for drop and bubble breakup in turbulent dispersions. *AIChE J.* **1996**, *42*, 1225–1233. [[CrossRef](#)]
27. Luo, H. *Coalescence, Breakup and Liquid Circulation in Bubble Column Reactors*; Norwegian Institute of Technology: Trondheim, Norway, 1993.

28. Yang, W.; Luo, Z.; Zhao, N.; Zou, Z. Numerical Analysis of Effect of Initial Bubble Size on Captured Bubble Distribution in Steel Continuous Casting Using Euler-Lagrange Approach Considering Bubble Coalescence and Breakup. *Metals* **2020**, *10*, 1160. [[CrossRef](#)]
29. Thomas, B.G.; Yuan, Q.; Mahmood, S.; Liu, R.; Chaudhary, R. Transport and entrapment of particles in steel continuous casting. *Metall. Mater. Trans. B* **2014**, *45*, 22–35. [[CrossRef](#)]
30. Wang, Y.; Fang, Q.; Zhang, H.; Zhou, J.; Liu, C.; Ni, H. Effect of argon blowing rate on multiphase flow and initial solidification in a slab mold. *Metall. Mater. Trans. B* **2020**, *51*, 1088–1100. [[CrossRef](#)]
31. Jiang, P.; Yang, J.; Zhang, T.; Xu, G.; Liu, H.; Zhou, J.; Qin, W. Optimization of flow field in slab continuous casting mold with medium width using high temperature measurement and numerical simulation for automobile exposed panel production. *Metals* **2019**, *10*, 9. [[CrossRef](#)]

Disclaimer/Publisher’s Note: The statements, opinions and data contained in all publications are solely those of the individual author(s) and contributor(s) and not of MDPI and/or the editor(s). MDPI and/or the editor(s) disclaim responsibility for any injury to people or property resulting from any ideas, methods, instructions or products referred to in the content.